Full length article

Transformation stress of shape memory alloy CuZnAl: Non-Schmid behavior

S. Alkan, Y. Wu, A. Ojha, H. Sehitoglu*

Department of Mechanical Science and Engineering, University of Illinois at Urbana-Champaign, 1206 W. Green Street, Urbana, IL 61801, USA

ARTICLE INFO

ABSTRACT

We establish an atomistically-informed model for predicting the non-Schmid behavior of critical stresses for bcc to orthorhombic ($L2_1$ to 18R) martensitic transformation in CuZnAl alloys. The interplay between the stacking fault displacements and the applied stress tensor components are shown to be responsible for the variation of the CRSS levels as much as a factor of almost 2.5 (25 MPa–60 MPa) depending on the crystal orientation. The predicted transformation stresses exhibit excellent agreement with the experimental results in this study and the measurements reported in the literature. The possible role of deviations from crystallographic ordering was also investigated illustrating the increase in transformation stress levels upon introduction of local disorder.

© 2017.

1. Introduction

The field of shape memory alloys (SMAs) is undergoing resurgence in the last ten years. This is due to the renewed consideration of SMAs that have the potential for elastocaloric effects for refrigeration [1–3], the need for better understanding of fatigue resistance [4,5] and the development of high temperature SMA capabilities [6]. It is the potential use of CuZnAl alloys in elastocaloric adiabatic cooling that has invigorated research in this class of alloys [7–9]. Though there are other alternate cooling methods utilizing the magnetocaloric [10,11] and electrocaloric [12,13] effects, these techniques fall short of the large temperature changes achieved with the SMAs. In the past studies, the Cu-based alloys have been the focus of the research groups in USA [14–17], Japan [18], Spain [19–21], Germany [22,23], France [24,25], Belgium [26,27] and Argentina [28]. The ternary CuZnAl alloys were one of the first SMAs that have been tested under different stress states [17,25], modeled with constitutive equations [24,29] and examined under fatigue (with multiple transformations) [23,30,31]. Despite this early enthusiasm, the attention has mostly veered towards the NiTi alloys clearly for potential biomedical applications [32,33]. On the other hand, for widespread applications in structures and components, the ternary CuZnAl alloy possesses favorable cost, excellent damping characteristics and the right attributes for excellent functionality [34,35]. For example, the low transformation stress for superelasticity relative to slip stress in CuZnAl presents a unique opportunity for engineering applications. The present experimental results show that the critical resolved shear stress (CRSS) for austenite slip exceeds 200 MPa in CuZnAl far exceeding the transformation stress of 25 MPa (<001> orientation). This large difference could lead to realization of improved functionality.

The superb superelasticity and shape memory behavior of CuZnAl has been documented previously [36]. From a functional performance perspective, CuZnAl exhibits transformation strains exceeding the well known NiTi [37]. Moreover, owing to its lower Clausius-Clapeyron (C-C) slope, the CuZnAl alloy can have a higher temperature range for superelasticity (200 °C) compared to NiTi (50 °C) [38]. On the other hand, to characterize the constitutive response of a shape memory alloy in a comprehensive fashion, one must understand at the foremost the magnitude of the transformation stress. Since the transformation energy pathways and the resulting shear-shuffle displacements are complex and dependent on the crystal structure, an accurate determination of transformation stress necessitates consideration of atomistic level mechanisms and their crystallographic correspondence. Examining the earlier literature evolved, it stands out that the majority of the efforts to quantify the critical transformation stress in the ternary CuZnAl alloy is limited to either a single orientation experiment or presumes the validity of Schmid Law, i.e. also known Critical Resolved Shear Stress-CRSS Law. Meanwhile, Schmid Law serves as a geometrical framework to quantify the critical transformation stress levels based solely on the contribution of glide stress component, this generalization is likely to introduce perplexities under different crystal orientations and loading states unless justified on theoretical and experimental grounds.

In particular, the earlier experimental measurements on the ternary CuZnAl alloy provide evidence for the anisotropic character of the CRSS for transformation, i.e. τ_{crit}^{trans}, which exhibit strong deviations from Schmid Law [29]. It is well known that CRSS for slip is a function of the crystal orientation and applied stress tensor in bcc,

B2, DO$_3$ and L2$_1$ ordered alloys [5,39,40]. Meanwhile, τ_{crit}^{trans} stands out as a paramount material parameter decisive on the functional performance of the CuZnAl shape memory alloy along with the transformation strain, a quantitative analysis has yet to be established for expounding upon its non-Schmid behavior under varying loading and sample orientations.

Accordingly, this work presents an atomistically-informed stacking fault mechanism for L2$_1$ to 18R transformation in CuZnAl alloy which can incorporate the dislocation core and applied stress tensor interplay prevalent in the lattice invariant shearing. Distinct from the earlier approaches, the present theoretical model can embrace the contribution of both shear and normal applied stress components to τ_{crit}^{trans} depicting a novel framework. The results demonstrate that τ_{crit}^{trans} exhibits a strong dependence on the crystal orientation under uniaxial loading conditions, introducing variations within a factor of almost 2.5 from the pure glide shear configurations. This variation in τ_{crit}^{trans} levels is of cardinal significance and should be an important consideration in design with shape memory alloys. From a broad perspective, building a comprehensive understanding for the anisotropic character of τ_{crit}^{trans} paves the way for promoting the performance of this class of functional alloys.

On theoretical grounds, a self-consistent framework has to be established based on the martensitic transformation energy pathway in conjunction with the corresponding cystallography. It is important to note that the composition and heat treatment can favor either DO$_3$ or L2$_1$ ordering, with a space group of Fm3m respectively, in the austenitic β phase in CuZnAl [28]. For the particular composition of Cu-27 at.%Zn-13.8 at.%Al focused in the present work, the L2$_1$ structure is favorable on thermodynamical grounds. Similarly, the martensites in CuZn and CuZnAl alloys may exhibit 2H, 3R, 9R, 18R, 6R crystal structures with different stacking sequences [20,28]. In alloys with an e/a concentration of 1.45–1.49 (such as in this study), the martensite has an 18R structure - denoted as β' phase [41]. For a brief overview of CuZnAl alloys and the transformation stress magnitudes as a function of composition and crystal structures, the reader is referred to Appendix A. Incorporating the preliminary crystallography information, we present a theoretical framework of the transformation energetics from the L2$_1$ austenite to 18R martensite structures via first principles methods (Density Functional Theory-DFT). These calculations will primarily focus on the prediction of the non-Schmid character τ_{crit}^{trans} by generating the transformation energy pathway as well as the role of deviations from long range order which is also observed to introduce local compositional change effects by changing the Al and Zn occupational sites [42]. The results demonstrate that the elevation in the transformation energy barriers can reach up to 50% with the introduction of disorder which serve as a prominent sign for the significance of the interatomic forces and energy barriers in the martensitic transformation.

On the whole, the theoretical framework established in this work, enables us to quantify the key parameters involved in the transformation energetics such as Burgers vector, shear moduli and energy barriers to manifest shear and shuffle mechanism from the first principles calculations, leading to the determination of the CRSS for transformation, τ_{crit}^{trans}. Within this context, nurturing these physical parameters as input for the meso-scale total energy formulation paves the way to explore the role of non-Schmid effects on the transformation stress in detail as well as pointing to the role of deviations from perfect order.

In summary, the aim of the present work is to establish the non-Schmid character of CRSS for martensitic transformation in CuZnAl, i.e. τ_{crit}^{trans}, on theoretical grounds without empiricism. To accomplish this task, a dislocation core mechanics formulation along with the

transformation energetics is established. The predicted anisotropic τ_{crit}^{trans} levels exhibit excellent agreement with the experimental measurements. Furthermore, we put special emphasis on the effect of ordering. The present analysis provides an effective methodology for tuning the functional performance of shape memory alloys by embracing the anisotropic behavior of critical transformation stress levels.

2. Simulation methods and results

2.1. Lattice structure calculations

In this section, we will present a theoretical framework to evaluate the transformation energetics/stress levels based on DFT calculations. To accomplish this task, the characterization of the physical parameters involved in generating the transformation energy profile of the ternary CuZnAl SMA such as the lattice constants of the austenite and martensite structures, the corresponding transformation path and the elastic moduli are the pre-requisites. This is a challenging task, especially for the ternary alloys such as CuZnAl, since the physical properties are highly sensitive to the composition and long-short range ordering effects. In the current work, we probe into L2$_1$ ordered and disordered configurations of CuZnAl alloy and establish a framework to evaluate the τ_{crit}^{trans} levels under uniaxial loading for varying crystallographic orientations. This physical framework allowed us to calculate the associated physical and mechanical parameters in excellent agreement with the experimental measurements.

The first-principles DFT calculations which are employed to determine the stable total structural energy as well as to generate the austenite to martensite transformation energy profile are implemented by utilizing Vienna ab initio Simulations Package (VASP) with the projector augmented wave (PAW) method within the framework of the generalized gradient approximation (GGA) [43,44]. This computation framework with PAW pseudopotentials can capture the valence electron effects which play a decisive role on the energetically favorable structures of alloys such as CuZnAl [45,46]. As a first step to simulate the physical response of the ordered CuZnAl crystalline in both austenitic and martensitic structures, a $2 \times 7 \times 2$ supercell with axes parallel to the cubic coordinate frame consisting of a total of 112 atoms is delineated. The Monkhorst Pack $12 \times 5 \times 12$ k-point meshing technique [47] was employed for the Brillouin-zone integration, and the convergence of the structural energy was verified to a tolerance level less than 10^{-5} eV via conjugate gradient algorithm ensuring the absolute value of the forces acting per atom is less than 5×10^{-3} eV/$\overset{\circ}{A}$.

Fig. 1 shows the configuration of the atoms for L2$_1$ ordered CuZnAl alloy employed in the DFT calculations. The occupation sites of the Cu atoms are positioned at odd-integer multiples of ($a_0/2,a_0/2,a_0/2$) sites meanwhile the sites at the integer multiples of a_0 along the cubic axes are shared among the Cu, Al and Zn atoms complying with the neutron diffraction data from the earlier literature [48]. As a first step, the lattice parameter of L2$_1$ ordered CuZnAl, $2a_0$, is varied such that the equilibrium lattice parameter is taken as the one that corresponds to the minimum structural energy. The resulting energy vs lattice parameter variation from the first-principles relaxation calculations are plotted in Fig. 1. From our calculations, $2a_0$, is determined as 5.828 $\overset{\circ}{A}$ which is in well agreement with the experimentally measured value of 5.846 $\overset{\circ}{A}$ [49]. Furthermore this lattice configuration corresponds to the lowest energy compared to the other possible configurations constructed by changing occupation sites of the Al and Zn atoms. To that end, the theoretical calculations will be
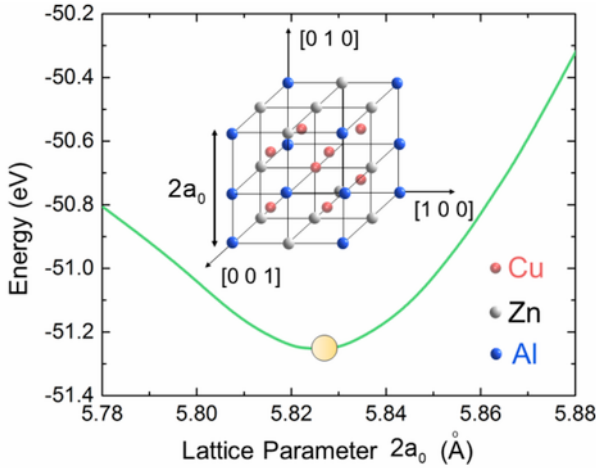
Fig. 1. Structural energy variation is plotted as a function of lattice parameter for the L2$_1$ order considered in the present study.

Fig. 2. Shows **(a)** the L2$_1$ structure of β and **(b)** 18R stacking of β' phases in CuZnAl. The stacking layers of B and C (B′ and C′) are distinguished by a translation of A (A′) row by a distance of a/3 and 2a/3 respectively in idealized positions neglecting the atomic radii and interaction effects. It is to be noted that the atomic neighboring between the two sets of stacking {A,B,C} and {A′, B′,C′} are different. To visualize the transformation shear, monoclinicity is conserved in the 18R structure meanwhile the same stacking can be also shown employing an orthorhombic cell.

furthered on the L2$_1$ ordered configuration of CuZnAl shown in Fig. 1 throughout the following sections.

The elastic constants of the austenitic CuZnAl are obtained by subjecting the volume of the minimum energy lattice configuration to the six independent distortional and dilatational strain components and tracking the energy variation response as function of applied strain. In the calculations, the strain levels are varied between −0.03 and 0.03 which ensures the elastic response for the imposed atomic displacements. The resultant independent elastic stiffness matrix components in cubic coordinate system shown in Fig. 1, i.e. denoted as C_{11}, C_{12} and C_{44} in Voigt notation, are established as 119, 107 and 90 GPa respectively which are consistent with the experimental values of 116, 102 and 84 GPa respectively [50,51].

Extending the atomistic scale structure calculations to the martensite lattice structure, within the nominal composition regime which we focus on, the earlier experimental measurements suggest that 18R orthorhombic martensitic structure exhibiting rhombohedral symmetry (indistinguishing the atomic order) is favored on energetics grounds [28]. At this stage, it is to be noted that 18R structured β' phase can be also described by a combination of 6 layered monoclinic unit cells, though the orthorhombic cell description employs a coordinate frame in which the c axis is perpendicular to the 18-layered periodic stacking [52]. To that end, we focused on the 18 layer periodic orthorhombic structure of the martensitic phase, i.e. 18 R (i.e. β' phase) and calculated the equilibrium lattice structure following a similar pathway as illustrated for the L2$_1$ ordered CuZnAl (i.e. β phase) in the previous sub-section.

The equilibrium martensite lattice structure inherited from the austenite phase β, (i.e. the configuration shown in Fig. 2) is constructed by employing the framework by Wechsler et al. [53], de Vos et al. [54] and Delaey et al. [55]. As can be seen in Fig. 2, the transformed layers along $[0\bar{1}1]$ direction follow a stacking order of $(2\bar{1})_6$ in Zhdanov notation [56]. The martensitic structure exhibits a lattice correspondence of $[100]_\beta \parallel [100]_{\beta'}$, $[010]_\beta \parallel [01\bar{1}]_{\beta'}$, and $[001]_\beta \parallel [011]_{\beta'}$ with the austenite phase [57]. The lattice constants corresponding to the martensitic β' phase are evaluated based on the first-principles calculations via delineating a 2×9 x 2 supercell by employing 12×12 x 12 k-points with a total of 144 atoms in the coordinate frame of $[011] - [\bar{1}00] - [0\bar{1}1]$. Following an energy minimization approach as detailed for the austenitic β phase, the lattice constants of the 18R structure, are evaluated as $a = 4.51\overset{o}{A}$,
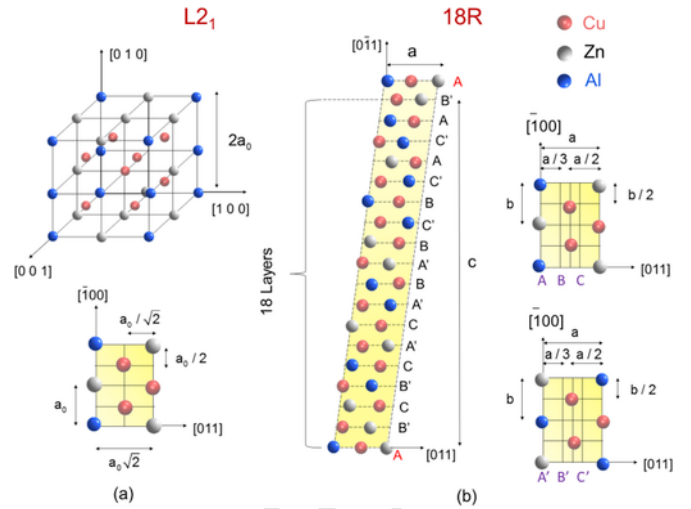
$b = 2.63\overset{o}{A}$ and $c = 38.4\overset{o}{A}$ which are in agreement with the earlier experimental measurements [49,58].

Following the perspective of crystallographic theory of martensitic transformations, the total deformation gradient can be expressed as the combined action of the rigid body rotation, the inhomogeneous lattice invariant shear (to ensure the existence of the undistorted habit planes) and the homogeneous Bain strain for the accurate lattice parameters [53]. On crystallographical grounds, the combined action of lattice invariant shear and Bain strain from L2$_1$ to 18R structure can be decomposed into three main steps: (i) a glide motion along every consecutive (011) $[0\bar{1}1]$ system (primary shear) to introduce close-packed structure, (ii) the shuffling of the atoms on the intermediate (011) layers in alternating directions to ensure the correct stacking order, and lastly (iii) a Bain strain which can be described as the compressive and tensile strains along the principal directions of $[00\bar{1}]$ and $[011]$ [59]. It is to be noted that the magnitude of the primary glide, i.e. $\delta_1 = |a_0/4[011]|$, is much greater than the shuffle distance δ_2 which will be evaluated within the framework of DFT in this section.

In order to determine the τ_{crit}^{trans} levels required to generate the equilibrium 18R martensite structure from the parent L2$_1$ lattice, we generated the transformation energy barrier curves resulting from the primary shear and shuffles as shown in Fig. 3. Meanwhile, the primary shear acting along every consecutive (011)[011] system overcomes the unstable stacking fault barriers of γ_{sd}^u as shown at the local maxima of the transformation energy curve, the alternating shuffling of the atoms on the intermediate planes introduces significant reduction as reflected by the local minima of stable stacking fault energy levels γ_{sd}^s. The resulting values for the unstable and stable energy path extrema values are tabulated in Table 1.

The low value of the shear modulus along (011) $[0\bar{1}1]$ shown in Table 3, i.e. $\mu_{\{110\} < 110>}$, favors the glide motion as (011) is also a potential slip plane for the L2$_1$ structure. As can be seen in Fig. 3, though the shuffling displacement of δ_2, i.e. of almost $a_0/16| < 110 >|$, is much smaller than the primary shear δ_1 , it con-
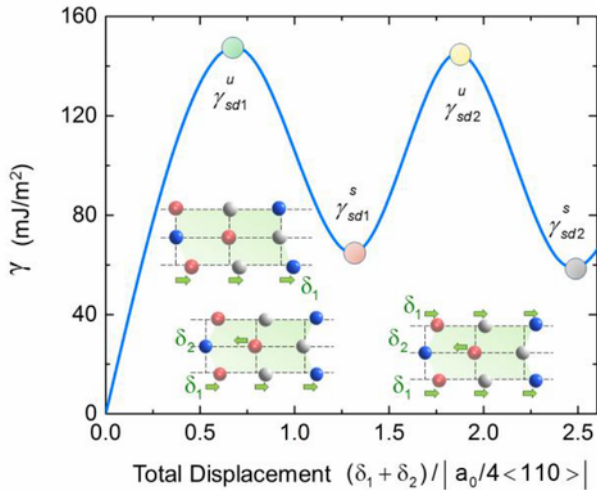
Fig. 3. The $L2_1$ to orthorhombic 18R transformation energy barrier is plotted. The energy levels for the formation of stacking faults are evaluated based within the framework of DFT imposing the primary shear and shuffle displacements of δ_1 and δ_2.

Table 1
The extrema of the transformation energy path of the GPFE curve, the shear moduli, the CRSS for transformation stress τ_{crit}^{trans} CuZnAl martensite.

γ_{sd1}^{u} mJm^{-2}	γ_{sd1}^{s} mJm^{-2}	γ_{sd2}^{u} mJm^{-2}	γ_{sd2}^{s} mJm^{-2}	$\mu_{\{110\}}<110>$ GPa	τ_{crit}^{trans} Exp. MPa	Theo.MPa
150	68	156	64	11	23	25

tributes to the relaxation of the faulted structure considerably with an energy level difference of almost $40\,mJ/m^2$ as can be seen in Fig. 3. A detailed analysis of the relaxed structure shows that the shuffled atoms are displaced along the complementary $\{110\}$ plane as shown in Fig. 4 for the imposed primary shear along $(0\bar{1}1)\,[011]$. This complies with the lower energy configuration of the stacking order of 18R [28].

Based on the lattice constants of the CuZnAl employed in this work, the stretches along the principle directions of $[00\bar{1}]$ and $[011]$ are equal to $\eta_1 = 0.911$ and $\eta_2 = 1.0681$ within the framework of the crystallographic theory of martensite [53,54]. These values correspond to a Bain strain with principal values of $\varepsilon_1 = -0.089$ and $\varepsilon_2 = 0.0681$. Following the construction of the atomistic-scale energy pathway, we will establish the theoretical framework for evaluating the τ_{crit}^{trans} levels which exhibit strong deviations from the Schmid Law as a result of the interplay between the stacking fault displacements and the applied stress tensor components in the next section.

2.2. Modelling non-Schmid transformation stress

In this section, we establish a dislocation-based model which can predict the τ_{crit}^{trans} levels as a function of the applied stress tensor and the crystallographic orientation in CuZnAl alloy. As $a_0/2 < 111 >$ dislocations are energetically favorable in β phase CuZnAl based on both Transmission Electron Microscopy (TEM) imaging studies and on theoretical grounds [60], the following dislocation dissociation reaction can introduce the primary shear:
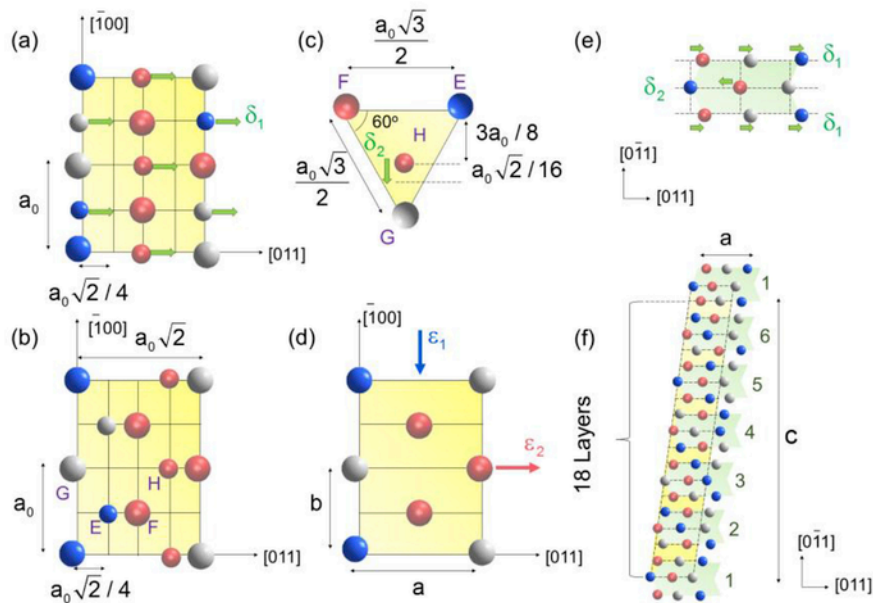

Fig. 4. Schematic illustrates the sequential shuffle and shear mechanisms for $L2_1$-18R transformation. **(a)** Shows the primary glide along $\delta_1 = a_0/4[011]$ on each consecutive $(0\bar{1}1)$ plane. The smaller atoms are located on a neighboring plane of $(0\bar{1}1)$. **(b)** the intermediate displaced positions of the atoms are shown in the undeformed coordinates. **(c)** Shows the secondary shuffling along the complimentary plane formed by E,F and G atoms as well as H atom on the top layer. It is to be noted that the atom H should be displaced by $\delta_2 = a_0/16[011]$ towards the G atom to ensure the close-packing. **(d)** Shows the accompanying principle Bain strain components, ε_1 and ε_2 which are evaluated to be as equal to -0.089 and 0.0681 from the phenomenological theory of martensite. **(e)** Shows the three layer formed as a result of primary shearing and the shuffling mechanism. **(f)** The 18R structure involves six of these packing layers shown in **(e)**.

$$\frac{a_0}{2}[111] \rightarrow \frac{a_0}{4}[011] + \frac{a_0}{4}[011] + \frac{a_0}{2}[100]$$

(1)

via the pair of $a_0/4[011]$ dislocations gliding on each consecutive (011) planes. This dissociation reaction along with the atomic shuffling of the intermediate layers in an alternating fashion can introduce the correct stacking order of the close-packed 18R structure meanwhile Bain deformation progresses with the aid of principle compressive/tensile strains driving the system into a local minimum energy, i.e. equilibrium configuration. It is to be noted that the dislocation reaction is energetically favorable based on Frank's rule [61]. Furthermore, earlier TEM imaging studies provide evidence for the presence of $a_0/2[111]$, $a_0/4[011]$ and $a_0/2[100]$ dislocations in samples with similar chemistry which have undergone pseudoelastic deformation cycles [62,63]. The relatively high density of $a_0/2[100]$ dislocations pinpointed in TEM images complies with the sessile character of these defects closely linked with the high energy barrier along $<001>\{110\}$ glide system on the generalized stacking fault surfaces of $L2_1$ ordered lattices [28]. The required stress to activate the dissociation reaction in Eq. (1) may either be imposed by the applied loading or may inherently exist as a result of internal stress fields in grain boundaries or defects acting as stress concentrators. Fig. 4 illustrates the construction of close-packed 18R structure from the $L2_1$ lattice with the proposed mechanism.

Modelling the variation of τ_{crit}^{trans} under a general applied stress tensor σ_{ij}, necessitates to quantify the total energy barrier incorporating the interaction of the two glissile fractionals of $a_0/4[011]$ and a sessile fractional of $a_0/2[100]$ based on the reaction expressed in Eq. (1). To accomplish this task, we described the spatial variation of the displacements associated with Burgers vectors of these three fractionals as a function of applied stress components including both glide (shear) and the non-glide (normal and shear) character. These displacement fields represent the distribution of slip along the corresponding glide planes as a function of spatial coordinate x and are denoted as disregistry functions $f_i(x)$ for i=1,2,3. Adopting the disregistry field definition for identifying the dislocations allows us to characterize the variation of τ_{crit}^{trans} as a function of single crystal orientation under uniaxial loading.

The disregistry functions of these three imperfect dislocations with Burgers vectors of $b_1 = a_0/4[011]$, $b_2 = a_0/2[100]$ and $b_3 = a_0/4[011]$ are established by employing the following form in Eq. (2) with the free coefficients of c_i and ξ_i (i=1,2,3) following Foreman et al. and Kroupa et al. [64,65]:

$$f_i(x) = \frac{b_i}{\pi}\left[\tan^{-1}\left(\frac{x}{c_i\xi_i}\right) + (c_i - 1)\xi_i\frac{x}{x^2 + (c_i\xi_i)^2}\right] + \frac{b_i}{2}$$

(2)

satisfying the conservation of Burgers vector condition described as:

$$\int_{-\infty}^{+\infty}\frac{\partial f_i}{\partial x}dx = b_i$$

(3)

The free coefficients c_i and ξ_i which are the characterizing parameters of the dislocation widths can be expressed as functions of the applied stress tensor, i.e. $c_i = c_i(\sigma_{ij})$ and $\xi_i = \xi_i(\sigma_{ij})$ ensuring the equilibrium, or in other words the minimum total energy configuration. To that end, we construct a total energy, E_{total}, formulation as a function of disregistry distributions under general applied loading conditions as such:

$$\begin{aligned}E_{total} &= E_{int} + E_{self} + E_\gamma^s - W \\ &= -\frac{K}{2\pi}\sum_{\substack{i=1 \\ i \neq j}}^{3}\int_{-\infty}^{+\infty}\frac{\partial f_i}{\partial x}\frac{\partial f_j}{\partial x}dx + N\frac{K}{2(1-v)}\left(1\right. \\ &\quad \left. - v\cos^2\theta\right)\sum_{i=1}^{3}\int_{-\infty}^{+\infty}\frac{\partial f_i}{\partial x}\frac{\partial f_i}{\partial x}dx \\ &\quad + \int_{-\infty}^{+\infty}\gamma[f(x)]dx \\ &\quad - N\sum_{i=1}^{3}\sigma_{ij}n_j\frac{1}{2}\left(m_in_k + m_kn_i\right)f_k\end{aligned}$$

(4)

where N is equal to 6 for the 18R martensitic structure. The anisotropic parameter K distinguishes the elastic shear moduli along the glide direction as the atomic lattice registry is not identical along $<110>$ and $<100>$. For planar slip distribution, K is equal to $\mu_{\{110\}<110>}$ and $\mu_{\{110\}<100>}$ which correspond to 11 and 27 GPa following the appropriate coordinate transformation of the 4th order elastic moduli tensor the principle values of which are already evaluated within the framework of first-principles calculations in section 2.1 [66]. The geometrical parameters m_j and n_k correspond to the jth and kth components of the normalized slip plane and direction vectors for the dislocations of b_1, b_2 and b_3 based on the dislocation reaction described in Eq. (1). The individual terms of E_{int}, E_{self}, E_γ^s and W represent the interaction and self-energies of the fractional dislocations, the short range misfit energy which evaluated based on the transformation energy surface constructed in Fig. 3 and the applied glide work on the dislocations respectively. Eq. (4) is solved for the functions of $f_i(x)$ minimizing the E_{total} expression under a given uniform applied stress. To find the local minima of the E_{total} expression, firstly we generated the set of the critical configurations under the ap-

plied stress as:

$$\frac{\partial E_{total}}{\partial f_i} = 0 \quad (i = 1, 2, 3)$$

(5)

Furthermore, to select the configurations corresponding to the local minima of E_{total}, we implemented the second partial derivative test which states that the Hessian matrix, H_{ij}, constructed as follows:

$$H_{ij} = \frac{\partial^2 E_{total}}{\partial f_i \partial f_j} \quad (i, j = 1, 2, 3)$$

(6)

should be semi-positive definite ensuring Eq. (5) is satisfied. On mathematical grounds, considering that H_{ij} is a symmetric real-valued matrix, this is equivalent to imposing the Sylvester's conditions [67]:

$$P_1 = H_{11} \geq 0$$

(7.a)

$$P_2 = \det\left(\begin{bmatrix} H_{11} & H_{12} \\ H_{21} & H_{22} \end{bmatrix} \right) \geq 0$$

(7.b)

$$P_3 = \det\left(H_{ij} \right) \geq 0$$

(7.c)

which primarily state that the principal minors P_1, P_2 and P_3 are to be positive at the local minima of E_{total} expression. For an applied stress tensor σ_{ij}, the functions $f_i(x)$ are constructed by evaluating c_i and ξ_i parameters from the set of equations expressed in Eq. (5) and Eq. (7).

The critical transformation stress is evaluated as the maximum gradient of the E_{total} expression normalized with respect to the glissile Burgers vector b_1 (or similarly b_3), i.e. following the Peierls-Nabarro framework [68], as expressed in Eq. (8):

$$\tau_{crit}^{trans} = \frac{1}{b_1} \max\left(\frac{\partial E_{total}}{\partial f_1} \right)$$

(8)

Fig. 5 illustrates the variation of disregistry distribution of the dissociated dislocations, b_1, b_2 and b_3, from the dislocation $a_0/2[111]$ for the <519> and <647> tension samples at the onset of glide. The variation in the intensity of the dislocation density distribution in Fig. 5 is described as:

$$\rho_i(x) = \frac{\partial f_i}{\partial x}$$

(9)

and it suggests that the non-glide shear and normal stress components participate effectively in the critical transformation stress level, i.e. τ_{crit}^{trans}. As can be seen in comparison with the orientations of <519> and <647>, complying with the magnitude of τ_{crit}^{trans}, the dislocation density of the glissile dislocations tends to decrease and the corresponding cores attain a planar structure exhibiting a lower glide resistance and promoting the primary shear. To that end, the planarity
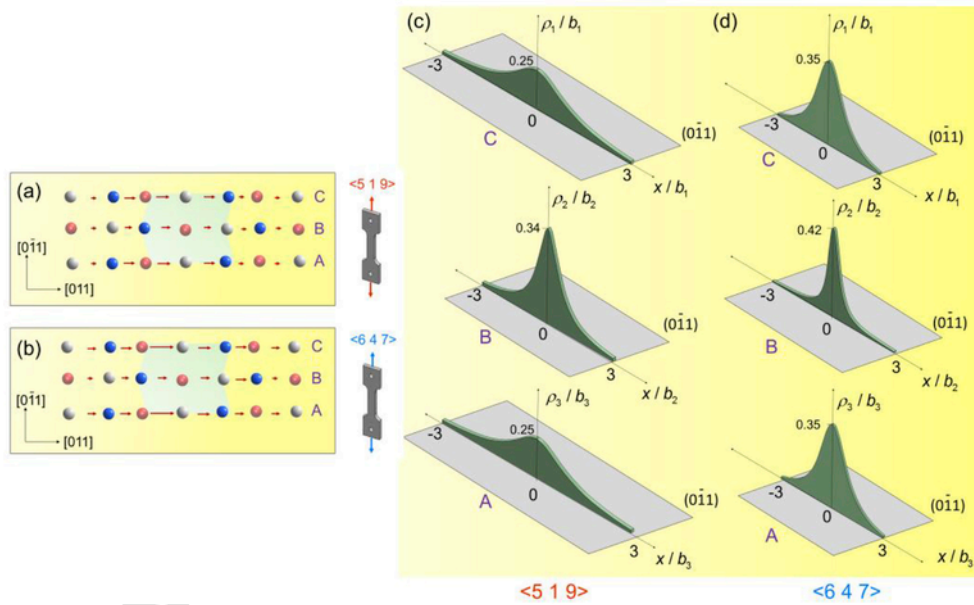

Fig. 5. (a) and (b) illustrates the atomistic scale relative displacements parallel to [011] along the (011) planes of C, B and A for the uniaxial tensile loading directions <519> and <647>. It is noted that they are normalized with respect to max{ρ_1,b_1}. (c) and (d) shows the resulting dislocation densities along the planes C, B and A for the uniaxial tensile directions along <519> and <647> respectively.

of the disregistry distributions for the primary shear is of paramount importance in the τ_{crit}^{trans} levels.

Table 2 tabulates the theoretical τ_{crit}^{trans} values for the onset of transformation based on Cu-27 at.%Zn-13.8 at.% Al composition. As can be seen, τ_{crit}^{trans} levels vary from 25 MPa to 55.2 MPa for the selected uniaxial tension orientations. The τ_{crit}^{trans} values in these orientations are tabulated on purpose of comparing the theoretical predictions with the experimental data of Lexcellent et al. [29] for Cu-23.7 at.%Zn-9.4 at.% Al single crystals under uniaxial tension. The differential between two set of data can be attributed to the composition differences as well as the treatment procedure followed as interatomic forces are demonstrated to govern on the GPFE energy levels followed through the transformation crystallography pathway.

Comparison with the experimental measurements along <001> as detailed in Appendix B, the predicted τ_{crit}^{trans} value of 25 MPa exhibits also an excellent agreement. The anisotropy in τ_{crit}^{trans} values of both compositions are very significant and stems from the coupling between the non-glide shear and normal components with the disregistry of primary shearing. At this stage it is to be emphasized that, the deviations from the Schmid law is not specific to CuZnAl alloy but is also present in other shape memory alloys such as NiTi [69–71] and NiFeGa [72] which follow a transformation path from B2 to B19′ and $L2_1$ to $L1_0$ respectively.

Fig. 6 (a) shows the variation of the τ_{crit}^{trans} levels under uniaxial loading directions projected on the stereographic triangle. Compared to the Schmid factor distribution shown in Fig. 6 (b), the resolved transformation shear stress levels exhibit significant differences ex-
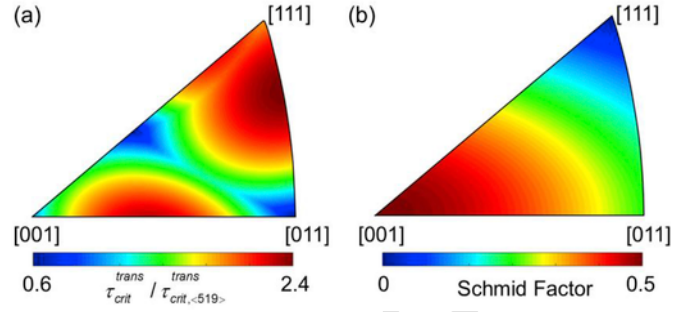

Fig. 6. (a) Shows the mapping of the anisotropic variation of the τ_{crit}^{trans} (normalized with the $\tau_{crit,<519>}^{trans}$ level for <519> tension) under crystallographic directions of uniaxial tension mapped on stereographic triangle. As can be seen, there is a significant anisotropy involved in the theoretical transformation stress levels complying with the experimental measurements in earlier literature [29]. (b) Shows the projection of the Schmid factor levels. Comparison between the stereographic projections of (a) and (b) exhibits very significant differences addressing the prevailing non-Schmid behavior of τ_{crit}^{trans} levels.

hibiting the non-Schmid character of the underlying physical phenomenon. The interplay between the fractionals of $a_0/2[100]$, $a_0/4[011]$ and the applied loading introduces factors of 0.6–2.4 in $\tau_{crit}^{trans}/\tau_{crit,<519>}^{trans}$ ratio as a function of uniaxial tension orientation on theoretical grounds ($\tau_{crit,<519>}^{trans}$ corresponds to the τ_{crit}^{trans} level for uniaxial tension along <519>).

2.3. Effect of crystallographic ordering

It is well known in the shape memory field that the state of long-range ordering facilitates transformation at low stress levels [35,74]. The crystal ordering combined with sufficiently high plastic slip resistance, allows accommodation of strain at the transformation interface in an elastic fashion and thus the reversibility is promoted. However, the deviations from perfect ordering are known to occur as a result of local clustering or heat treatment effects [28]. It is demonstrated that the τ_{crit}^{trans} and M_s temperature of β phase ternary CuZnAl alloy is also affected by the deviations from the perfect long-range ordering [42]. To that end, a $3 \times 7 \times 2$ supercell consisting of 168 atoms was employed within the framework of the first-principles DFT calculations for simulating CuZnAl crystalline with various local composition ratios of Cu, Zn and Al in the disordered crystalline configuration. The disordered crystal is delineated by assigning the positions of Cu, Zn and Al in the supercell employing a random generator code in MATLAB as shown in Fig. 7. The cell size employed in first-principles calculations is confirmed to be sufficient for the convergence of the resulting lattice parameters and the transformation energy curves.

In determination of the lattice parameters and the transformation energy barriers of disordered crystalline, special emphasis is put on the local clustering effects of Zn and Al as the change in their occupational sites from the perfect $L2_1$ order is known to introduce variations in τ_{crit}^{trans} (or M_s) on experimental grounds [42]. As the transformation energy barrier levels are highly sensitive to the local neighboring of the atoms, the supercells corresponding to the three disordered crystalline configurations, i.e. denoted as S_1, S_2 and S_3, are divided into three regions-Regions I, II and III as shown in Fig. 7. Meanwhile, the disordered Region I and Region III obey the nominal composition of Cu-27 at.%Zn-13.8%Al for each configuration, in Region II where the stacking fault is introduced during the transformation process, the composition is changed to Cu-27 at.% Zn- 33 at.%

Table 2
The variation of τ_{crit}^{trans} (MPa) with the single crystal loading direction in Cu-23.7 at.%Zn-9.4 at.%Al from the literature [29] and the theoretical predictions based on the composition of Cu-27 at.%Zn-13.8 at.%Al (this study) are tabulated at room temperature-RT. The 'T' and 'C' abbreviations denote tension and compression respectively. In this study, we conducted uniaxial loading experiments on [001] T and [001] C samples which are also included in Table 2. For comparison, the anisotropic behavior of transformation stress in 50.8% at.Ni- NiTi [69–71] and Ni-19 at.%Fe −27 at.% Ga [72,73] single crystals are also tabulated. The theoretical calculations of the present study are presented in bold face.

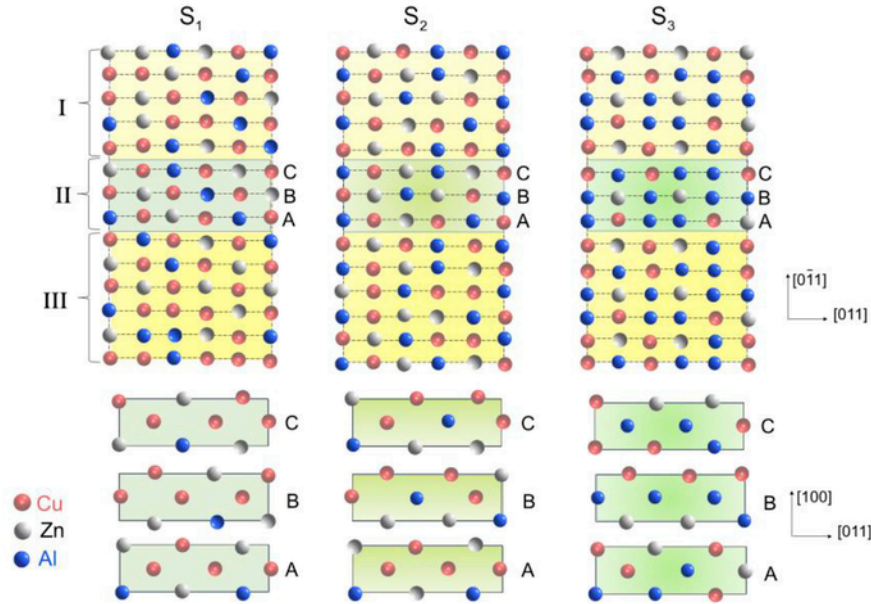| Alloy	<001> T	<001>C	<5 1 9> T	<8 4 9> T	<1 0 3> T	<17 0 19> T	<6 4 7> T
Cu-27Zn-13.8Al τ_{crit}^{trans} RT **Theory, This Study**	**25** (23 Exp.)	**25** (23 Exp.)	**25**	**33**	**39.7**	**41**	**55.2**
Cu-23.7Zn-9.4Al τ_{crit}^{trans} (Exp.) RT [29]	–	–	29.5	48.4	50.7	51.9	70.8
		<001>C	<148>C	<011> T	<112>C	<111>C
50.8 Ni-Ti τ_{crit}^{trans} (Exp.) RT [69–71]		132	144	157	226	138
		<001>T	<001>C		<123> C	
Ni-19Fe-27Ga τ_{crit}^{trans} (Exp.) 100 °C [72]		56	101		92	
		<001> T	<011>T		<123>T	
Ni-19Fe-27Ga τ_{crit}^{trans} (Exp.) 25 °C [73]		35	23.5		18	

Fig. 7. Shows the disordered crystalline of S_1, S_2 and S_3 with the planar stacking within the fault zone (colored in green). (For interpretation of the references to colour in this figure legend, the reader is referred to the web version of this article.)

Al and Cu- 16% Zn-55 at.% Al for the S_2 and S_3 disordered crystals. The composition of Cu-27 at.%Zn-13.8%Al in Region II is preserved for S_1 configuration. This local composition change within the neighborhood of the stacking fault enables us to quantify the effect of Al and Zn contents near the fault plane as illustrated in Fig. 7 as well as distinguishing between the disorder and local clustering effects. From the structural energy relaxation calculations similar to the perfectly order configuration in section 2.1, the average lattice constant is determined to be equal to $2a_0 = 5.84$ $\overset{\text{o}}{\text{A}}$ for the disordered configurations of S_1, S_2 and S_3 in which case $2a_0 = 5.87$ $\overset{\text{o}}{\text{A}}$, $2a_0 = 5.82$ $\overset{\text{o}}{\text{A}}$ and $2a_0 = 5.85$ $\overset{\text{o}}{\text{A}}$ respectively. Furthermore, Table 3 tabulates the γ_{sd1}^{s} levels for these three configurations.

Following the total energy formulation introduced in Eq. (4), τ_{crit}^{trans} values are calculated for the disordered S_1, S_2 and S_3 states. Table 4 shows the variation of the corresponding τ_{crit}^{trans} values for each disordered configuration of <001> tension sample. As can be seen, the disordered S_1 phase is conducive to transform at a slightly higher level of CRSS than the perfect ordered L2$_1$. The formation of faults as an internal strain relaxation mechanism with the deviation

Table 3
The corresponding γ_{sd1}^{s} values in mJm^{-2} for the three configurations S_1, S_2 and S_3. It is to be emphasized that the local chemistry varies from the overall composition in Region II of S_2 and S_3 configurations as tabulated.

Configuration	Composition in Region II	γ_{sd1}^{s} mJm^{-2}
S_1	Cu-27 at.%Zn-13.8%Al	86
S_2	Cu-27 at.% Zn-33 at.% Al	92
S_3	Cu- 16% Zn-55 at.% Al	95

Table 4
Shows the variation of τ_{crit}^{trans} (in MPa) for perfect ordered configuration (i), and the disordered S_1, S_2 and S_3 crystallite for <001> orientation.

	S_1	S_2	S_3
Perfect L2$_1$ order			
25	28	30	33

from the perfect ordering underscores this behavior complying with the electron microscopy studies [16,75,76]. To that end, formation of the faults introduce a higher energy cost against the primary shearing at the onset of transformation. On the other hand, the calculated τ_{crit}^{trans} levels for S_2 and S_3 configurations demonstrate that the local clustering of Zn and Al has a greater contribution in the elevation of τ_{crit}^{trans} compared to the disordering with the conserved chemical composition.

3. Discussion of results

The transformation stress magnitude of CuZnAl along <001> loading orientation is remarkably low (τ_{crit}^{trans}= 23 MPa in uniaxial tension or compression) which is predicted by the proposed theory. The experimental values correspond to temperatures of approximately 25 °C. At higher temperatures, τ_{crit}^{trans} stresses increase proportionally with increasing temperature obeying C-C rule. The habit plane variants established from phenomenological theory correspond closely with the observations from the Digital Image Correlation (DIC) traces which are detailed in Appendix B in Figure B2. As the transformation stress is exceeded, the martensite domains grow and engulf a large fraction of the specimen. Such a transformation proceeds at constant stress in tension over a stress plateau [77]. The high reversibility is closely linked with the difference between τ_{crit}^{trans} (25 MPa) and τ_{crit}^{slip} (200 MPa) for <001> compression sample as the accommodation of transformation strains inside the austenitic β phase in an elastic fashion is promoted with high slip resistance.

The transformation from a cubic ($L2_1$) to orthorhombic (18R) lattice structure is accomplished via combined action of shear-shuffle along $\{110\} \langle 110 \rangle$ systems. At this stage, it should be noted that this mechanism exhibits a strong similarity with the bcc to hcp transformation observed in Ti-Ta and Ti-Nb shape memory alloys which have been interrogated in a recent study by our group [78]. The transformation path from an open bcc lattice in the austenite phase to the closed-packed 18R martensite phase involves displacements that can be associated with either the dislocation core displacements or phonon softening along $(0\bar{1}1)\,[011]$ crystallographic direction [79–81]. As the dislocation glide motion is governed by both glide and non-glide stress components of the applied stress tensor components in bcc derivative lattices, including $L2_1$ structure, the deviations from the Schmid Law are expected to prevail on τ_{crit}^{trans} levels [5,40,82]. At this stage, it is important to emphasize that the disregistry displacements which are quantified based on the energy minimization framework, play key a role in capturing the deviations from the transformation pathway imposed by the lattice geometry employed in the ab-initio calculations under general applied stress states. To this end, the predictive model presented in this work can embrace the contribution of glide and non-glide applied stress components on the transformation pathway.

Up to date, no profound discussion of the deviations from Schmid law in Cu-based shape memory alloys has been provided and CuZnAl shape memory alloy is no exception as it has been demonstrated to exhibit a strong deviation from Schmid behavior both on experimental [29] and theoretical grounds. The current quantitative analysis elucidates on the dissociation of the $a_0/2[111]$ dislocation into two glissile $a_0/4[011]$ partials which impart the necessary primary transformation shear as well as a sessile $a_0/2[100]$ partial interacting with the other partials. The resulting dislocation densities of the three fractional dislocations that contribute to the total energy expression in Eq. (4) exhibit an interplay with the applied stress tensor components. To that end, τ_{crit}^{trans} levels show significant variations in conjunction with the behavior of these three fractionals and the applied stress tensor components.

Both theoretical predictions and the experimental measurements point to the elevated resistance against $L2_1$ to 18R transformation near the [011]-[111] poles of the stereographic triangle compared to the [001] pole as demonstrated in Table 2 and Fig. 6. The anisotropic variation of τ_{crit}^{trans} has important implications in designing with shape memory alloys as the functional performance of this class of materials depends on mainly two quantities: the transformation stress and the transformation strain. Meanwhile, the crystal orientation dependence of the transformation strain is well established, the orientation dependence of the transformation stress is equally important but has not been well understood. The current study presents a novel atomistically-informed mechanistic approach to establish the anisotropic character of τ_{crit}^{trans} in close agreement with the experimental measurements.

As the data tabulated in Table 2 suggest that the deviations from Schmid Law in τ_{crit}^{trans} levels under varying crystallographic loading orientation is not unique to CuZnAl alloy but also observed in other shape memory alloys including NiTi and NiFeGa [70–72]. On the other hand, the extent of the anisotropy involved in τ_{crit}^{trans} levels is strongly dependent on the composition, the transformation energy barrier and the crystallographic pathway followed *en-route* to martensitic transformation. To this end, different constitutive response is expected for each shape memory alloy even though non-Schmid behavior of τ_{crit}^{trans} prevails at the onset of martensitic transformation. The origin of the anisotropy in shape memory alloys emanates from several factors: the anisotropy of elastic constants, the anisotropy of the transformation strains, the anisotropy of slip resistance (stress) and the anisotropy of transformation stress. The latter two effects are not as well-known and has been a topic of emphasis in our recent work. Specifically, the anisotropy of transformation stress is the focus in this paper. The transformation stress anisotropy can itself be considered due to two factors: (i) different martensite habit plane variants activated in tension-compression or crystal orientation, and (ii) the non-Schmid effects in transformation stress because during the lattice invariant shearing, the accommodating dislocation core disregistry distribution may interact with the applied stress state. It is the non-Schmid effect (ii) that is the topic of this paper. In other words, the coordinated motion of the lattice points mapping the parent phase to the product phase can be expressed as disregistry displacements which exhibit strong interplay with both the glide and non-glide stress components. Specifically, we characterized the anisotropy involved in τ_{crit}^{trans} levels in CuZnAl alloy based on a defect mechanics model fostered with the ab-initio transformation energy barrier calculations. If one were to examine finite temperature effects, we draw attention to the C-C equation which incorporates the entropy change and the transformation strain which is also orientation dependent. On the other hand, to study finite temperature effects, transformation entropy needs to be available from experiments because its theoretical determination is still in its infancy.

We note that the coordinated motion of the lattice points mapping the parent phase to the product phase can be expressed as disregistry displacements of dislocation core spreading and in various shape memory materials (including B2, DO_3 and $L2_1$ ordered) they are known to exhibit strong interplay with both the glide and non-glide stress components. Such an anisotropy at lattice resistance dominates the response near the transformation equilibrium temperature. In fact its role can even extend to elevated temperatures depending on the efficacy of the C-C effect.

To provide further evidence, we note similar trends in another shape memory alloy, $Ni_{54}Fe_{19}Ga_{27}$ (at. %) shown in Figure C1 of Appendix C. At 25 °C under superelastic conditions with $L2_1$ to $L1_0$ martensitic transformation, the CRSS levels for transformation, τ_{crit}^{trans}, are determined to be as 18 MPa, 23.5 MPa and 35 MPa for <123>, <011> and <001> uniaxial tension samples respectively. These experimental measurements provide evidence for the non-Schmid behavior of transformation stress in NiFeGa alloy resulting from the interaction between the applied stress components (both glide and non-glide) for each loading orientation. These results are obtained near Af and can not be attributed to the C-C effect because the transformation strains in tension for <123> and <001> are 7% and 12% respectively. Hence, the C-C slope is higher for the <123> case by nearly 1.7 times. Yet, the experimental results show lower a CRSS value for <123> compared to <001>. Clearly, in this case the lattice resistance effects (i.e. non-Schmid effect) are dominating compared to the C-C effect. As the test temperature is increased the C-C effects become more significant and the CRSS for <123> at 100 °C (Table 2) shows the highest value.

For shape memory alloys where the C-C slopes are rather low such as the case of low entropy change or high transformation strains (FeMnNiAl alloys for example), the lattice resistance effect is expected to dominate. But, the data for FeMnNiAl for comparison are non-existent at the moment. For other alloys with higher entropy change, at temperatures near the M_d temperature, the C-C effects could dominate. But this is a regime that is not well studied since it is not well suited for practical applications.

In recent years, a rich literature has evolved around the debate on the role of internal residual stress development on shape memory re-

sponse [83]. Such internal stresses have been attributed to the non-homogeneity of transformation which are closely linked with the associated defect mechanics. Inevitably, the internal stresses factor into the overall performance by altering the functionality (hysteresis, response over time, transformation strains) as well as the fatigue and fracture behavior of shape memory alloys. The anisotropic τ_{crit}^{trans} levels play an important role in the variation of fatigue life as a function of sample orientation [63,84]. Furthermore, the results affect the micro-mechanical modeling efforts involving texture effects on transformation response and ultimately implementation of such models in finite element analysis. In conjunction with these arguments, the demonstrated anisotropic character of τ_{crit}^{trans} in the current work presents a strong motivation to incorporate the significant deviations from the Schmid law in crystal plasticity models.

There has been considerable debate regarding the role of ordering in CuZnAl alloys. Our initial calculations have been conducted in L2$_1$ ordered state of CuZnAl. The deviations from the perfect ordering is expected to shift the slip stresses to smaller magnitudes hence curtailing the efficacy of these alloys. On the other hand, the transformation stress magnitudes (especially associated with shuffle barriers) would increase with the degree of disorder, hence closing the gap between slip and transformation stresses as shown in this work.

We note that the CuZnAl alloy, which exhibits excellent superelasticity, can undergo two mechanisms that has hampered its wide spread application. The first of these mechanisms is the martensite stabilization introduced by pinning of thermally induced martensite interfaces formed upon quenching below M_s by the quenched-in defects such as vacancies and partial dislocations [85]. The quenched-in defects hinder the austenite-martensite interface motion and increases the reverse transformation temperatures of A_s and A_f limiting the shape memory response [27]. At this stage it is to be emphasized that the maximum degree of ordering is not achieved under such conditions increasing the thermal hysteresis [28,86]. In this study, the martensite stabilization effects are minimized by quenching above M_s temperature which promotes L2$_1$ austenitic structure. The favorable heat treatments undertaken in this work are also reflected by the low thermal hysteresis of 25 °C, i.e. $A_f - M_f$ [38,87]. This behavior is closely related to the changes in the packing factor of the martensitic 18 R structure and the concentration differential of vacancies with the degree of ordering [88,89].

As the second mechanism, grain growth which can adversely affect the functionality of such alloys [90] and has been controlled with addition of grain refining elements. Since the experiments conducted in this study are focused on single crystals with clearly no grain boundary effects, the grain growth mechanism is not a factor. Furthermore, the use of single crystals results in a clear identification of the habit plane variants and allows the Schmid factors for all potential variants to be determined.

4. Conclusions

The work supports the following conclusions:

(1) The CuZnAl alloys exhibit low transformation stress (CRSS) levels varying from 25 to 60 MPa depending on the crystal orientation. Although there is a significant variation as a function of crystal and loading orientation as we show, these levels are substantially lower than the CRSS for slip stress near 200 MPa. The wide differential between the critical slip and transformation stresses facilitate reversibility.

(2) The transformation path from austenite to martensite was achieved via a shear and shuffle mechanism on the alternating {110} planes.

(3) A dislocation based mechanism has been established to generate the shear displacements required during transformation. The interplay between the core spreading and the applied loading is shown to be responsible for the significant deviations of the critical transformation stress from Schmid law.

(4) The digital image correlation-DIC permits precise determination of the resolved stress corresponding to the martensitic transformation from L2$_1$ to 18R structures. The transformation habit planes observed via DIC are in agreement with the predicted habit planes which allows the CRSS levels to be extracted precisely.

(5) Introduction of crystallographic disorder in the simulations resulted in an increase of the transformation energy barrier from 68 to 86–96 mJ/m^2 as well as increasing the critical transformation stress from 25 MPa to 33 MPa for <001> sample under tension. The results confirm that fully ordered crystals produce the most favorable conditions-lowest transformation stresses well below the slip stress.

Appendix A. Brief overview of CuZnAl alloys

Within the last three decades, a rich literature evolved around the identification of the transformation behavior in the ternary CuZnAl alloy employing single crystals. Upon surveying the critical transformation stress for different CuZn and CuZnAl compositions, it is found that the Cu-27 at.%Zn-13.8 at.%Al alloy shows one of the lowest transformation stresses (50 MPa uniaxial stress level for <001> orientation) compared to other compositions, and is chosen as the material in the current study [36,38,91]. To precisely identify the onset of strain gradients in habit plane variant(s) corresponding to transformation nucleation and pinpoint the corresponding transformation stress, in this work, *in-situ* DIC technique is implemented on <001> single crystals under uniaxial tension-compression. The details of the methodology adopted for the experimental measurements are described in Appendix B. To distinguish the on-set of transformation and slip-mediated plasticity, different heat treatment paths are followed. Furthermore, slip trace analyses have been conducted under optical microscope and employing Scanning Electron Microsopy (SEM) to determine the active variants for the transformation cases. The distinguishingly low level of transformation stress of 25 MPa plays a decisive role for a 9% recoverable tensile strain complying with the superior shape memory properties of CuZnAl.

It is important to identify the composition dependence of the austenite and martensite crystal structures to set the proper background for this work and the experimentally measured transformation stress levels. The martensite of CuZn and CuZnAl alloys may exhibit 3R, 9R, 18R, and 6R long period layered rhombohedral structures with different stacking sequences or 2H hexagonal martensite structures depending on the electron-atom (e/a) concentration and composition [18,28,92–95]. At a high e/a concentration (1.45–1.49), the martensite exhibits an 18R structure derived from an ordered L2$_1$ or DO$_3$ CuZnAl austenite [20,28]. It is important to note that single crystal Cu-27 at.%Zn-13.8 at.%Al alloy in this study has an e/a ratio equal to 1.45 which results in an 18R structure. For this composition, we note that the monoclinic angle is close to 90°, and hence the martensite can be approximated as an orthorhombic crystal. While

the alloy with an e/a ratio below 1.42 shows the 3R structure, at intermediate e/a values, the martensite is characterized by the coexistence of both 3R and 9R martensite structures as shown in earlier experiments on binary Cu-37.7 at.%Zn and Cu-37.6 at.%Zn alloys [96,97]. At a very high e/a concentration, 2H martensites are formed which are usually brittle [57] and not very useful. The 2H martensites are found in ternary CuZnAl alloys with high Al content. Similarly, the 3R martensite appears in CuZnAl alloys with low Al content, and is derived from the A2 disordered or B2 ordered austenite. The CuZnAl alloys that undergo bcc-18R transformation exhibit superelasticity, and are commonly pursued in the scientific community due to their technological importance.

The commonly used shape memory alloys (for example, NiTi with the exception of R phase formation in special cases and Ti-based alloys) exhibit a single stage transformation (i.e. from austenite phase to one martensite phase). In CuZnAl two stage transformation is possible from $L2_1$ (or DO_3) to 18R and 18R to 6R, however the stress required to induce the second transformation can be high and close to the CRSS for slip [98]. To that end, in this work, the attention has been focused on the CuZnAl compositions with a single stage transformation. In the alloy composition and treatment employed in this work, the $L2_1$ ordered austenite phase firstly transforms into the 18R martensite.

With the crystallographic morphology, there is a need to develop models that could capture transformation stresses without empirical assumptions. This is the subject of the current paper. Such an approach will not only assess the shape memory performance of the current CuZnAl alloys, but it will also assist future alloy design by highlighting the complex crystal transformation paths, and identify the roles of ordered/disordered structures on the transformation stress level-a key quantity in SMAs. Hence, the present study is expected to fill a gap in treatment of CuZnAl class of SMAs.
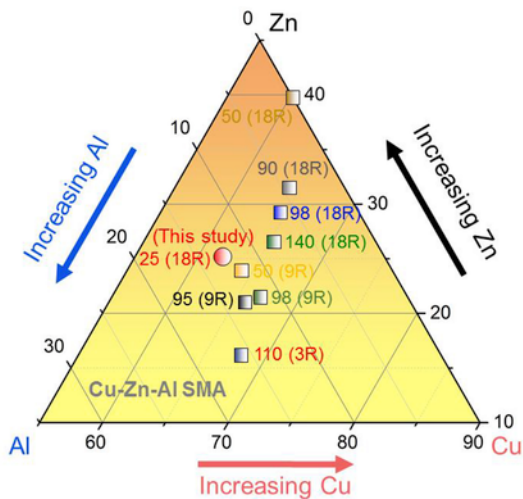

Fig. A1. Ternary plot showing the critical transformation stress for different compositions of CuZnAl alloys. The composition of Zn ranges from (15–27) at.% and Al content ranges from (4–14) at.% [18,28,92–95].

Appendix B. Experimental methods and results

In the present study, the [001] oriented CuZnAl single crystals with a composition of Cu-27 at.%Zn-13.8 at.%Al are utilized. The [001] loading orientation of the single crystals experimented is cho-

sen on the fact that this direction theoretically yields the highest transformation strain under uniaxial stress which permits the visualization of the local strain fields employing DIC technique. The samples are solutionized at 800 °C for 30 min followed by water quench and then heat treated at 80 °C for 24 h before being subjected to furnace cooling. The transformation temperatures are determined as $A_s = 4$ °C, $A_f = 13$ °C, $M_s = 1$ °C, $M_f = -12.5$ °C by the Differential Scanning Calorimetry measurements at a scan rate of 40 °C/min as shown in Fig. 1.
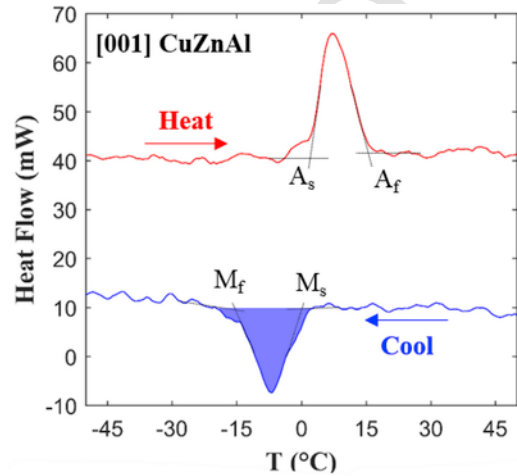

Fig. B1. Differential Scanning Calorimetry measurements conducted for determining the transformation temperatures are plotted.

Regarding the crystallographic symmetry involved in the martensitic transformation of the ternary CuZnAl alloy studied in the current work, there are 24 possible variants that can be activated based on the single crystal orientation and the applied loading state. Each particular variant is related to the rest of the variants via appropriate orthogonal rotation matrices. The habit planes separating the parent austenite phase from the activated variant are tabulated in Table 1. It should be emphasized that the habit planes are of undistorted character ensuring the crystallographic correspondence between the parent and the martensite phases.

Table B1 tabulates the 24 possible habit planes associated with the enumerated variants which belong to the {0.6243 0.2436 0.7422} family.

V1	(-0.6243,-0.2436,0.7422)	V9	(0.7422,0.6243,0.2436)	V17	(0.6243
V2	(-0.2436,-0.6243,-0.7422)	V10	(0.7422,-0.6243,-0.2436)	V18	(-0.624
V3	(0.6243,0.2436,0.7422)	V11	(-0.7422,-0.2436,-0.6243)	V19	(0.2436
V4	(0.2436,0.6243,-0.7422)	V12	(-0.7422,0.2436,0.6243)	V20	(-0.243
V5	(-0.6243,0.2436,-0.7422)	V13	(-0.7422,0.6243,0.2436)	V21	(0.6243
V6	(0.2436,-0.6243,0.7422)	V14	(-0.7422,-0.6243,0.2436)	V22	(-0.624
V7	(0.6243,-0.2436,-0.7422)	V15	(0.7422,0.2436,-0.6243)	V23	(-0.243
V8	(-0.2436,0.6243,0.7422)	V16	(0.7422,-0.2436,0.6243)	V24	(0.2436

The orientation of the samples are analyzed employing Electron Backscatter Diffraction (EBSD) prior to any mechanical deformation. The resulting orientation mapping is plotted employing inverse stereographic projection in Fig. 2 (a). Based on this crystallographic orientation of the samples loaded under tension and compression, the projected slip traces of the habit planes on the DIC tracking surface with normal along Z direction Fig. B2(a) is schematized in Fig. B2(b). In

addition to analyses on DIC strain localizations and optical surface trace analyses, the two-surface trace analyses are also employed via SEM to determine the activated variants. The analysis for [001] compression sample is illustrated in Fig. B2 (c) and (d) for the (-X) and (Z) surfaces respectively. The SEM imaging analyses demonstrate that only single variants of V1 and V4 are activated for [001] uniaxial tension and compression samples respectively.
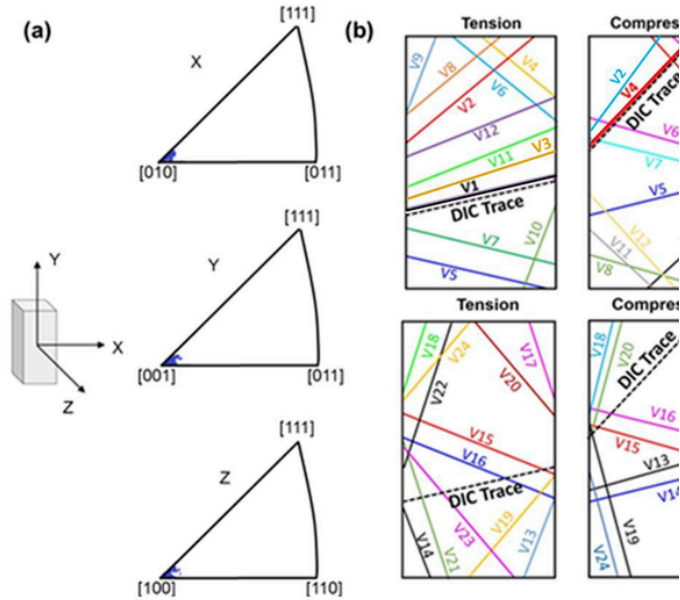

Fig. B2. (a) The stereographic triangle projections of the [001] sample crystallographic orientations determined via EBSD analysis. **(b)** The comparison of the projected habit planes on Z surface of the sample along with the experimentally observed axial strain DIC traces are schematized in scale. This geometrical trace analysis enables to identifying the activated variants in uniaxial tension and compression, respectively. **(c)** Shows the SEM image taken at the surface of compression sample with normal directed along <Z>. V4= (0.2436, 0.6243, −0.7422) variant is determined to be active on this surface. **(d)** Shows the SEM image taken at the surface of the compression sample with normal directed along <-X>.Similarly, V4= (0.2436, 0.6243, −0.7422) variant is determined to be also active on this surface. These experimental results comply with the predictions of the theoretical framework established.

The uniaxial stress vs strain curves of [001] single crystal samples in tension and compression are shown in Fig. B3 and B4 respectively. As can be seen, this selected orientation produces a recoverable transformation strain of nearly 9% in tension and 6% in compression. Close examination of the projected transformation front planes indicate that the activated variant pairs are V1 and V4 under tension and compression respectively. The transformation habit planes conform to the traces predicted based on the phenomenological theory ({0.6243 0.2435 0.7421} family) as shown in Fig. B4 and B5. The full recovery of the stress-strain curves indicate that slip mediated plasticity accompanying the transformation front motion is of negligible effect. The dislocation mediated slip will introduce macroscopic irreversible strains which stem from the unsynchronized glide response of the interface dislocations with the martensitic transformation front motion as detailed in a recent review by Chowdhury et al. [4].

At this stage, it is important to emphasize that the number of favorable variants under [001] uniaxial loading is 4 in Schmid law and

3 in our predictive model. On the other hand, slight variations from the [001] direction not extending 4.5° which is satisfied by our EBSD mapping analyses, result in a single active variant in our theoretical framework. Our model encompassing the non-glide stresses can predict the experimentally observed variants of (−0.6243,-0.2436,0.7422), V1, and (0.2436, 0.6243, −0.7422), V4, under tension and compression respectively. In contrast, the Schmid law predicts equally probable two variants with habit planes of (−0.6243,-0.2436, 0.7422) and (0.6243,-0.7422,+0.2436), V1 and V17, for this zone under uniaxial tension as well as (−0.2436,-0.6243, −0.7422) and (0.2436,0.6243,-0.7422), V2 and V4, for this zone under uniaxial compression. This result addresses the significant contribution of non-glide stresses on the activation pathway of the distinct martensite variants as a function of uniaxial loading orientation. However, this does not rule out the fact that further experimental measurements with loading directions spanning a rich portion of the stereographic triangle are to be conducted in the prospective studies to elaborate on the role of non-glide stresses in active variant selection and the corresponding transformation strain distribution.
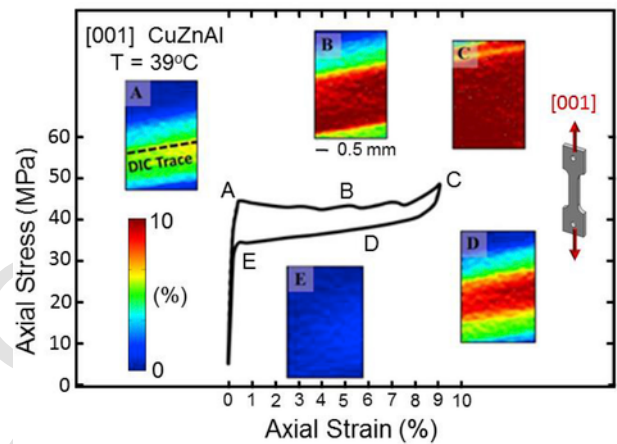

Fig. B3. Superelastic response of a [001] oriented Cu-27 at.%Zn-13.8 at%Al crystal deformed in tension.
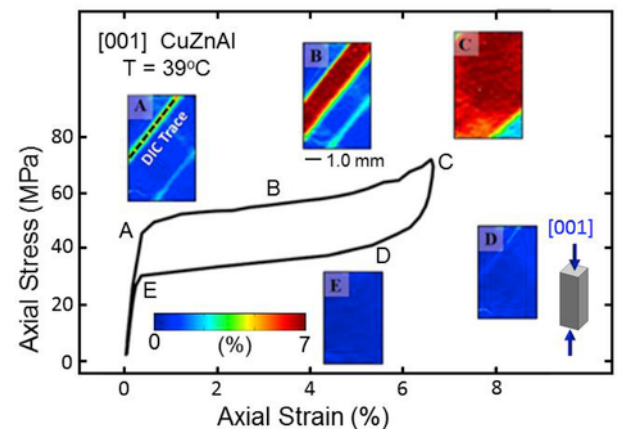

Fig. B4. Superelastic response of a [001] oriented Cu-27 at.%Zn-13.8 at%Al crystal deformed in compression.

On experimental grounds, the critical resolved transformation stress (τ_{crit}^{trans}) is determined to be 23 MPa in tension and compression which is the CRSS level acting along the {110} <110> system determined based on the following transformation direction and plane analysis within the framework of first-principles presented in Section 2. At this stage, it is to be noted that owing to the asymmetric nature of transformation mechanisms, different variants are activated under tension and compression. In this case, the agreement of the calculated transformation orientation and experiments is excellent.

In order to develop a further comparative understanding on the transformation and slip stress levels in the CuZnAl alloy, the stress vs strain curve under uniaxial compression along [001] direction is plotted in Fig. B5. The onset of slip occurs at point A along $(\bar{1}\bar{1}2)$ [111] entailing a Schmid factor of 0.47; thus, we establish the CRSS for slip, τ_{crit}^{slip}, as slightly above 200 MPa. The comparison of τ_{crit}^{slip} and τ_{crit}^{trans} which are of nearly 200 and 23 MPa respectively, suggests that the crystal resistance against slip is much greater than it is for transformation. Therefore, the transformation may proceed at stress levels far below the slip stress which complies with the reversible character of the stress vs strain curves under tension and compression in Fig. B3 and B4.
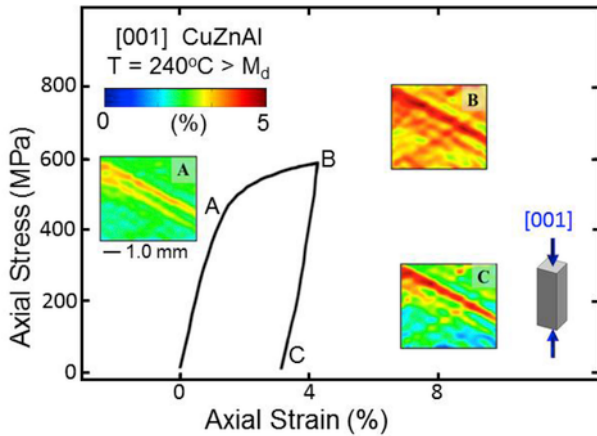
Fig. B5. The stress-strain response of [001] crystal at temperatures where plastic flow occurs.

Appendix C.

In order to establish a solid understanding on the deviation of τ_{crit}^{trans} from Schmid law in numerous shape memory alloys and to instigate further attention for the prospective studies, in this appendix section, we will expound upon the experimental measurements of Ni-19Fe-27Ga (at.%) shape memory alloy under uniaxial tension for three distinct orientations, i.e. <100>, <011> and <123> at 25 °C. The details of these presented experimental stress-strain curves can be found in the earlier work by Prof. Sehitoglu and his students [73]. As shown in Fig. C1, τ_{crit}^{trans} levels are measured to be as 18 MPa, 23.5 MPa and 35 MPa in <123>, <011> and <001> samples for $L2_1$ to $L1_0$ martensitic transformation in Ni-19Fe-27Ga. Considering the 100% difference between <123> and <001> under tension (18 vs 35 MPa), the non-Schmid character of the τ_{crit}^{trans} is substantial and should be incorporated into any modelling and design efforts in Ni-19Fe-27Ga similar to other alloys in Table 2.
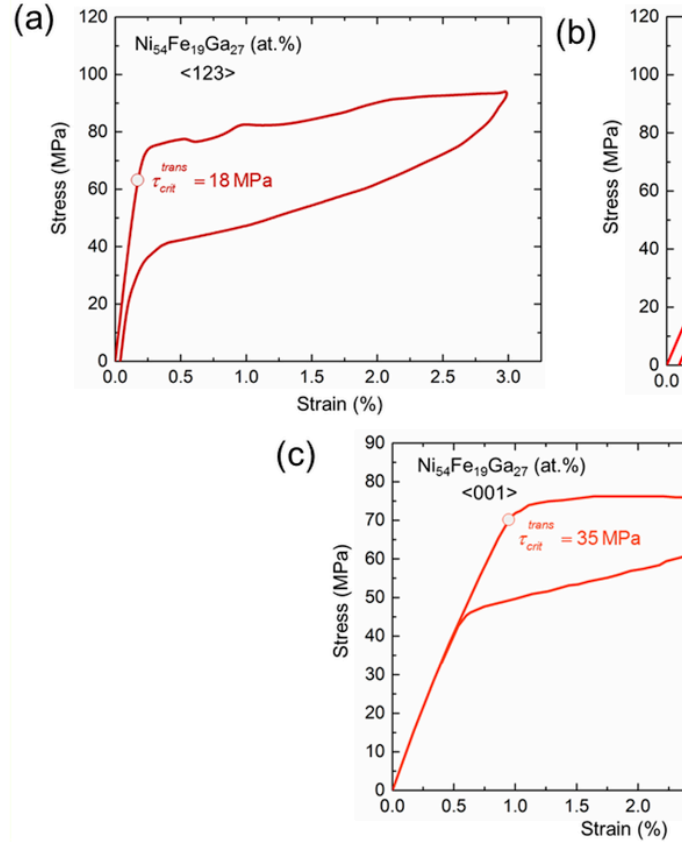
Fig. C1. **(a)** Stress vs strain curves of unaged NiFeGa shape memory alloy under uniaxial tension and compression along <123> crystal orientation. **(b)** Stress vs strain curves of unaged NiFeGa shape memory alloy under uniaxial tension and compression along <011> crystal orientation. **(c)** Stress vs strain curves of unaged NiFeGa shape memory alloy under uniaxial tension and compression along <001> crystal orientation. All results are for room temperature.

References

[1] L. Mañosa, A. Planes, Materials with giant mechanocaloric effects: cooling by strength, Adv. Mater. (2016).

[2] G.J. Pataky, E. Ertekin, H. Sehitoglu, Elastocaloric cooling potential of NiTi, Ni 2 FeGa, and CoNiAl, Acta Mater. 96 (2015) 420–427.

[3] P. Chowdhury, H. Sehitoglu, Deformation physics of shape memory alloys – fundamentals at atomistic frontier, Prog. Mater. Sci. 88 (2017) 49–88.

[4] P. Chowdhury, H. Sehitoglu, A revisit to atomistic rationale for slip in shape memory alloys, Prog. Mater. Sci. 85 (2017) 1–42.

[5] S. Alkan, H. Sehitoglu, Dislocation core effects on slip response of NiTi- a key to understanding shape memory, Int. J. Plast. 97 (2017) 126–144.

[6] J. Ma, I. Karaman, R.D. Noebe, High temperature shape memory alloys, Int. Mater. Rev. 55 (2010) 257–315.

[7] L. Mañosa, S. Jarque-Farnos, E. Vives, A. Planes, Large temperature span and giant refrigerant capacity in elastocaloric Cu-Zn-Al shape memory alloys, Appl. Phys. Lett. 103 (2013), 211904.

[8] E. Bonnot, R. Romero, L. Mañosa, E. Vives, A. Planes, Elastocaloric effect associated with the martensitic transition in shape-memory alloys, Phys. Rev. Lett. 100 (2008), 125901.

[9] L. Mañosa, D. González-Alonso, A. Planes, E. Bonnot, M. Barrio, J.-L. Tamarit, S. Aksoy, M. Acet, Giant solid-state barocaloric effect in the Ni-Mn-In magnetic shape-memory alloy, Nat. Mater. 9 (2010) 478–481.

[10] A. Smith, C.R.H. Bahl, R. Bjørk, K. Engelbrecht, K.K. Nielsen, N. Pryds, Materials challenges for high performance magnetocaloric refrigeration devices, Adv. Energy Mater. 2 (2012) 1288–1318.

[11] X. Moya, L.E. Hueso, F. Maccherozzi, A.I. Tovstolytkin, D.I. Podyalovskii, C. Ducati, L.C. Phillips, M. Ghidini, O. Hovorka, A. Berger, M.E. Vickers, E. Defay, S.S. Dhesi, N.D. Mathur, Giant and reversible extrinsic magnetocaloric effects in La0.7Ca0.3MnO3 films due to strain, Nat. Mater. 12 (2013) 52–58.

[12] X. Moya, S. Kar-Narayan, N.D. Mathur, Caloric materials near ferroic phase transitions, Nat. Mater. 13 (2014) 439–450.

[13] S.-G. Lu, Q. Zhang, Electrocaloric materials for solid-state refrigeration, Adv. Mater. 21 (2009) 1983–1987.

[14] T. Schroeder, C. Wayman, Pseudoelastic effects in Cu- Zn single crystals, Acta Metall. 27 (1979) 405–417.

[15] J. Perkins, Shape Memory Effects in Alloys, Springer Science & Business Media, 2012.

[16] M.H. Wu, J. Perkins, C.M. Wayman, Long range order, antiphase domain structures, and the formation mechanism of α1 ("Bainite") plates in A Cu-Zn-Al alloy, Acta Metall. 37 (1989) 1821–1837.

[17] K. Gall, K. Jacobus, H. Sehitoglu, H.J. Maier, Stress-induced martensitic phase transformations in polycrystalline CuZnAl shape memory alloys under different stress states, Metall. Mater. Trans. A 29 (1998) 765–773.

[18] T. Saburi, Y. Inada, S. Nenno, N. Hori, Stress-induced martensitic transformations in Cu-Zn-Al and Cu-Zn-Ga alloys, J. Phys. Colloq. 43 (1982), C4–633-C634-638.

[19] J. Vinals, V. Torra, A. Planes, J.L. Macqueron, Effect of atomic order on the thermodynamic properties of the martensitic transformation in CuZn and CuZnAl alloys, Philos. Mag. A: Phys. Condens. Matter. Struct. Defects Mech. Prop. 50 (1984) 653–666.

[20] F. Gil, J. Guilemany, The determination of the electron to atom ratio interval corresponding to the change in the martensitic structure from α′ to β′ in Cuznal shape memory alloys, Mater. Res. Bull. 27 (1992) 117–122.

[21] J. Pons, M. Sade, F. Lovey, E. Cesari, Pseudoelastic cycling and two-way shape memory effect in β Cu–Zn–Al alloys with γ-precipitates, Mater. Trans., JIM 34 (1993) 888–894.

[22] M. Thumann, E. Hornbogen, Thermal and mechanical fatigue in Cu-base shape memory alloys, Zeitschrift fur Metallkunde 79 (1988) 119–126.

[23] M. Sade, E. Hornbogen, Fatigue of single- and polycrystalline -CuZn-base shape memory alloys, Zeitschrift fur Metallkunde 79 (1988) 782–787.

[24] E. Patoor, M. El Amrani, A. Eberhardt, M. Berveiller, Determination of the origin for the dissymmetry observed between tensile and compression tests on shape memory alloys, J. Phys. IV 5 (1995), C2-495-C492-500.

[25] A. Vivet, C. Lexcellent, Observations and analysis of martensitic phase transformation on CuZnAl single crystals, J. Phys. IV 9 (1999), Pr9-411-Pr419-418.

[26] H. Warlimont, L. Delaey, Martensitic transformations in Cu-, Ag- and Au-Based alloys, Prog. Mater. Sci. 1974 (18) (1974) 160.

[27] L. Delaey, J. Van Humbeeck, M. Chandrasekaran, J. Janssen, M. Andrade, N. Mwamba, Cu-Zn-Al shape memory alloys, Met. Forum 4 (1981) 164–175.

[28] M. Ahlers, Martensite and equilibrium phases in Cu-Zn and Cu-Zn-Al alloys, Prog. Mater. Sci. 30 (1986) 135–186.

[29] C. Lexcellent, B.C. Goo, Q.P. Sun, J. Bernardini, Characterization, thermomechanical behaviour and micromechanical-based constitutive model of shape-memory Cu-Zn-Al single crystals, Acta Mater. 44 (1996) 3773–3780.

[30] K.N. Melton, O. Mercier, Fatigue life of CuZnAl alloys, Scripta Metall. 13 (1979) 73–75.

[31] M. Sade, C. Damiani, R. Gastien, F.C. Lovey, J. Malarría, A. Yawny, Fatigue and martensitic transitions in Cu–Zn–Al and Cu–Al–Ni single crystals: mechanical behaviour, defects and diffusive phenomena, Smart Mater. Struct. 16 (2007) S126.

[32] D. Stoeckel, Nitinol medical devices and implants, Minim Invasive Ther. Allied Technol. 9 (2000) 81–88.

[33] T.,M.S. Yoneyama, Shape Memory Alloys for Biomedical Applications, Woodhead Publication, 2009.

[34] J. Van Humbeeck, Damping capacity of thermoelastic martensite in shape memory alloys, J. Alloy. Comp. 355 (2003) 58–64.

[35] K. Otsuka, C.M. Wayman (Eds.), Shape Memory Materials, Cambridge University Press, Cambridge, 1998.

[36] T. Saburi, C. Wayman, K. Takata, S. Nenno, The shape memory mechanism in 18R martensitic alloys, Acta Metall. 28 (1980) 15–32.

[37] F.D.C. Bubani, M. Sade, F. Lovey, Improvements in the mechanical properties of the 18R↔6R high-hysteresis martensitic transformation by nanoprecipitates in CuZnAl alloys, Mater. Sci. Eng., A 543 (2012) 88–95.

[38] Y. Wu, E. Ertekin, H. Sehitoglu, Elastocaloric cooling capacity of shape memory alloys – role of deformation temperatures, mechanical cycling, stress hysteresis and inhomogeneity of transformation, Acta Mater. 135 (2017) 158–176.

[39] R. Gröger, A.G. Bailey, V. Vitek, Multiscale modeling of plastic deformation of molybdenum and tungsten: I. Atomistic studies of the core structure and glide of 1/2 <111> screw dislocations at 0K, Acta Mater. 56 (2008) 5401–5411.

[40] S. Alkan, H. Sehitoglu, Non-Schmid response of Fe 3 Al: the twin-antitwin slip asymmetry and non-glide shear stress effects, Acta Mater. (2017).

[41] J. Pelegrina, M. Ahlers, The martensitic phases and their stability in Cu-Zn and Cu- Zn- Al alloys—I. The transformation between the high temperature β phase and the 18R martensite, Acta Metall. Mater. 40 (1992) 3205–3211.

[42] A. Planes, R. Romero, M. Ahlers, The martensitic transition temperature in ternary Cu-Zn-Al alloys. Influence of the L21 structure, Acta Metall. Mater. 38 (1990) 757–763.

[43] G. Kresse, J. Furthmüller, Efficient iterative schemes for ab-initio total-energy calculations using a plane-wave basis set, Phys. Rev. B 54 (1996) 11169–11186.

[44] G. Kresse, J. Hafner, Ab initio molecular dynamics for open-shell transition metals, Phys. Rev. B 48 (1993) 13115–13118.

[45] P.E. Blöchl, Projector augmented-wave method, Phys. Rev. B 50 (1994) 17953–17979.

[46] G. Kresse, D. Joubert, From ultrasoft pseudopotentials to the projector augmented-wave method, Phys. Rev. B 59 (1999) 1758–1775.

[47] H.J. Monkhorst, J.D. Pack, Special points for Brillouin-zone integrations, Phys. Rev. B 13 (1976) 5188–5192.

[48] G. Ciatto, P.L. Solari, S. De Panfilis, A.L. Fiorini, S. Amadori, L. Pasquini, E. Bonetti, Atomic ordering in CuZnAl shape memory alloys investigated via x-ray absorption and diffraction, Appl. Phys. Lett. 92 (2008), 241903.

[49] G. Guenin, R. Pynn, D.R. Jara, L. Delaey, F.P. Gobin, Lattice dynamics of Cu-Zn-Al martensite, Phys. Status Solidi (a) 59 (1980) 553–556.

[50] Y. Wu, A. Ojha, L. Patriarca, H. Sehitoglu, Fatigue crack growth fundamentals in shape memory alloys, Shape Mem. Superelasticity 1 (2015) 18–40.

[51] A. Nagasawa, T. Makita, Y. Takagi, Anharmonicity and martensitic phase transition in β-phase alloys, J. Phys. Soc. Jpn. 51 (1982) 3876–3881.

[52] N. Zenji, K. Setsuo, Electron microscope study of the crystal structure of the martensite in a copper-aluminium alloy, Jpn. J. Appl. Phys. 2 (1963) 478.

[53] M.S. Wechsler, D.S. Lieberman, T.A. Read, On theory of formation of martensite, J. Met. 5 (1953) 1503–1515.

[54] J. De Vos, E. Aernodout, L. Delaey, The crystallography of the martensitic transformation of B. C. C. Into 9 R: a generalized mathematical model, Zeitschrift fur Metallkunde 69 (1978) 438–444.

[55] L. Delaey, M. Chandrasekaran, M. Andrade, J. Humbeeck, Non-Ferrous Martensites - Classification, Crystal Structure, Morphology, Microstructure, 1982.

[56] M. De Graef, M.E. Mchenry, Structure of Materials: an Introduction to Crystallography, Diffraction and Symmetry, Cambridge University Press, 2007.

[57] H. Warlimont, L. Delaey, Chapter 1 introduction, Prog. Mater. Sci. 18 (1974) 1–146.

[58] P.L. Rodriguez, F.C. Lovey, G. Guenin, J.L. Pelegrina, M. Sade, M. Morin, Elastic constants of the monoclinic 18R martensite of a Cu-Zn-Al alloy, Acta Metall. Mater. 41 (1993) 3307–3310.

[59] M. Ahlers, The martensitic transformation: a model, Zeitschrift fur Metallkunde 65 (1974) 636–642.

[60] P.L. Rodriguez, A.M. Condo, F.C. Lovey, Quantitative analysis of dislocations in relation with the martensitic transformation in Cu-Zn-Al alloys, physica status solidi (b) 197 (1996) 279–292.

[61] W.F. Hosford, Physical Metallurgy, Taylor & Francis, 2005.

[62] M. Sade, A. Uribarri, F. Lovey, An electron-microscopy study of dislocation structures in fatigued Cu-Zn-Al shape-memory alloys, Philos. Mag. A 55 (1987) 445–461.

[63] J. MalarríA, M. Sade, F. Lovey, Microstructural evolution in the pseudoelastic cycling of Cu–Zn–Al single crystals: behavior at a transition stage, Mater. Sci. Eng., A 308 (2001) 88–100.

[64] A.J. Foreman, M.A. Jaswon, J.K. Wood, Factors controlling dislocation widths, In: Proceedings of the Physical Society. Section A, vol. 64, 1951, p. 156.

[65] F. Kroupa, L. Lejček, Splitting of dislocations in the Peierls-Nabarro model, Czech. J. Phys. B 22 (1972) 813–825.

[66] A.J.E. Foreman, Dislocation energies in anisotropic crystals, Acta Metall. 3 (1955) 322–330.

[67] F. Csaki, A concise proof of Sylvester's theorem, Period. Polytech. - Electr. Eng. 14 (1970) 105.

[68] J.W. Christian, V. Vítek, Dislocations and stacking faults, Rep. Prog. Phys. 33 (1970) 307.

[69] H. Sehitoglu, I. Karaman, R. Anderson, X. Zhang, K. Gall, H.J. Maier, Y. Chumlyakov, Compressive response of NiTi single crystals, Acta Mater. 48 (2000) 3311–3326.

[70] K. Gall, H. Sehitoglu, Y.I. Chumlyakov, Y.L. Zuev, I. Karaman, The role of coherent precipitates in martensitic transformations in single crystal and polycrystalline Ti-50.8at%Ni, Scripta Mater. 39 (1998) 699–705.

[71] K.A. Gall, The Effect of Stress State and Precipitation on Stress-induced Martensitic Transformations in Polycrystalline and Single Crystal Shape Memory Alloys: Experiments and Micro-mechanical Modeling, University of Illinois, 1998.

[72] R.F. Hamilton, C. Efstathiou, H. Sehitoglu, Y. Chumlyakov, Thermal and stress-induced martensitic transformations in NiFeGa single crystals under tension and compression, Scripta Mater. 54 (2006) 465–469.

[73] C. Efstathiou, H. Sehitoglu, P. Kurath, S. Foletti, P. Davoli, Fatigue response of NiFeGa single crystals, Scripta Mater. 57 (2007) 409–412.

[74] K. Otsuka, A. Saxena, J. Deng, X. Ren, Mechanism of the shape memory effect in martensitic alloys: an assessment, Phil. Mag. 91 (2011) 4514–4535.

[75] M. Andrade, M. Chandrasekaran, L. Delaey, The basal plane stacking faults in 18R martensite of copper base alloys, Acta Metall. 32 (1984) 1809–1816.

[76] L. Delaey, I. Cornelis, The variation of stacking order and structure-symmetry in copper-base martensites, Acta Metall. 18 (1970) 1061–1066.

[77] I. Cornelis, C.M. Wayman, Phase Transformations in Metastable β′ CuZn Alloys: I: Martensitic Transformation, 1973.

[78] A. Ojha, H. Sehitoglu, Critical stress for the bcc–hcp martensite nucleation in Ti–6.25at.%Ta and Ti–6.25at.%Nb alloys, Comput. Mater. Sci. 111 (2016) 157–162.

[79] A. Planes, L. Mañosa, E. Vives, Vibrational behavior of bcc Cu-based shape-memory alloys close to the martensitic transition, Phys. Rev. B 53 (1996) 3039–3046.

[80] A. Planes, L. Mañosa, E. Vives, Vibrational behaviour of Cu-Based BCC alloys, J. Phys. IV France 05 (1995), C8–829-C828-834.

[81] M. Born, K. Huang, Dynamical Theory of Crystal Lattices, Clarendon Press, 1998.

[82] M.S. Duesbery, V. Vitek, Plastic anisotropy in b.c.c. transition metals, Acta Mater. 46 (1998) 1481–1492.

[83] P. Sedmák, P. Šittner, J. Pilch, C. Curfs, Instability of cyclic superelastic deformation of NiTi investigated by synchrotron X-ray diffraction, Acta Mater. 94 (2015) 257–270.

[84] J. Malarría, M. Sade, The effect of temperature on pseudoelastic cycling of Cu-Zn-Al single crystals, Scripta Metall. Mater. 30 (1994) 241–246.

[85] S. Kustov, S. Golyandin, K. Sapozhnikov, E. Cesari, J. Van Humbeeck, R. De Batist, Influence of martensite stabilization on the low-temperature non-linear anelasticity in Cu-Zn-Al shape memory alloys, Acta Mater. 50 (2002) 3023–3044.

[86] N. Kuwano, C.M. Wayman, Some effects of parent phase aging on the martensitic transformation in a Cu- AI- Ni shape memory alloy, Metallurgical Transactions A 15 (1984) 621–626.

[87] Z. Wei, D. Yang, On the hysteresis loops and characteristic temperatures of thermoelastic martensitic transformations, Scripta Metall. 22 (1988) 1245–1249.

[88] O. Adigüzel, Martensite ordering and stabilization in copper based shape memory alloys, Mater. Res. Bull. 30 (1995) 755–760.

[89] R. Rapacioli, M. Ahlers, The influence of short-range disorder on the martensitic transformation in Cu-Zn and Cu-Zn-Al alloys, Acta Metall. 27 (1979) 777–784.

[90] R. Elst, J. Van Humbeeck, L. Delaey, Grain growth behaviour of hot deformed beta-phase Cu-based alloys with second phase particles, In: Proc of the Riso Int Symp on Metall and Mater Sci 7th, Annealing Processes, Recovery, Recryst and Grain Growth, September 8, 1986-September 12, 1986, Riso Natl Lab, Roskilde, Den, 1986, pp. 309–313.

[91] E. Bonnot, R. Romero, X. Illa, L. Mañosa, A. Planes, E. Vives, Hysteresis in a system driven by either generalized force or displacement variables: martensitic phase transition in single-crystalline Cu-Zn-Al, Phys. Rev. B 76 (2007), 064105.

[92] R. Romero, M. Ahlers, On the martensitic transformation temperature and its stress dependence in Cu-Zn and Cu-Zn-Al single crystals, J. Phys. Condens. Matter 1 (1989) 3191.

[93] R. Romero, M. Ahlers, The influence of β-phase plastic deformation on the martensitic transformation in Cu-Zn-Al single crystals, Philos. Mag. A 59 (1989) 1103–1112.

[94] W. Arnedo, Instituto de Matemática, Astronomía y Física de la Universidad Nacional de Córdoba, Argentina, Thesis 1982.

[95] H. Sato, K. Takezawa, S. Sato, Two-step stress-induced martensitic transformation, In: Cu-Zn-Al Alloy Single Crystals, Science Reports of the Research Institutes, Tohoku University, 1981, pp. 85–90.

[96] I. Cornelis, C.M. Wayman, Phase transformations in metastable β′ CuZn alloys—I. Martensitic transformations, Acta Metall. 22 (1974) 291–300.

[97] H. Pops, T.B. Massalski, Thermoelastic and burst-type martensites in copper-zinc beta-phase alloys, Transact. Metallurg. Soc. AIME 230 (1964) 1662–1668.

[98] D. Ríos-Jara, G. Guénin, On the characterization and origin of the dislocations associated with the two way memory effect in Cu-Zn-Al thermoelastic alloys-I. Quantitative analysis of the dislocations, Acta Metall. 35 (1987) 109–119.